

## Investigation of noise generation by a model propeller in turbulent inflow through advanced signal processing techniques

Quaroni, L.N.; Sinnige, T.; Merino Martinez, R.

**DOI**

[10.2514/6.2025-3147](https://doi.org/10.2514/6.2025-3147)

**Publication date**

2025

**Document Version**

Final published version

**Published in**

AIAA aviation forum and ASCEND 2025

**Citation (APA)**

Quaroni, L. N., Sinnige, T., & Merino Martinez, R. (2025). Investigation of noise generation by a model propeller in turbulent inflow through advanced signal processing techniques. In *AIAA aviation forum and ASCEND 2025* Article AIAA 2025-3147 (AIAA Aviation Forum and ASCEND, 2025).  
<https://doi.org/10.2514/6.2025-3147>

**Important note**

To cite this publication, please use the final published version (if applicable).  
Please check the document version above.

**Copyright**

Other than for strictly personal use, it is not permitted to download, forward or distribute the text or part of it, without the consent of the author(s) and/or copyright holder(s), unless the work is under an open content license such as Creative Commons.

**Takedown policy**

Please contact us and provide details if you believe this document breaches copyrights.  
We will remove access to the work immediately and investigate your claim.



# Investigation of noise generation by a model propeller in turbulent inflow through advanced signal processing techniques

L. N. Quaroni\*, T. Sinnige<sup>†</sup> and R. Merino-Martínez<sup>‡</sup>

*Faculty of Aerospace Engineering, Delft University of Technology, 2629 HS Delft, the Netherlands*

The far-field acoustic emissions of an isolated scale-model propeller ingesting turbulent inflow are experimentally investigated in wind-tunnel measurements. Phase-averaging and phase-shifting signal processing techniques are used to separate the deterministic (tonal) and random (broadband) components of the recorded sound signals. It is reported that a combination of the two techniques prevents tones unrelated to the shaft rotational frequency from contaminating the estimate of the broadband part of the signal. Scaling and directivity analyses of the obtained broadband component highlight the presence of two noise generation regimes depending on the considered frequency range. In particular, a quasi-omnidirectional directivity pattern is observed for frequencies for which the Helmholtz number is much lower than unity when turbulence is ingested. On the other hand, a dipole-like pattern with minima close to the propeller's rotational plane gradually appears for higher frequencies. A time- and frequency-domain analysis through the Continuous Wavelet Transform (CWT) method shows how the increase in broadband noise is due to a large number of short-duration pulses linked to the ingestion of turbulence.

## List of relevant symbols

$A_{ext}$	=	$\pi D_{ext}^2/4$ , additional contraction exit area, [m <sup>2</sup> ]
$A_{flow}$	=	$\beta A_{wt}$ , flow area through turbulence grids, [m <sup>2</sup> ]
$A_p$	=	$\pi D_p^2/4$ , propeller disk area, [m <sup>2</sup> ]
$A_{wt}$	=	$\pi D_{wt}^2/4$ , wind tunnel exit nozzle area, [m <sup>2</sup> ]
$B$	=	number of blades, [-]
$c_\infty$	=	speed of sound in the freestream, [m/s]
$c_{0.7}$	=	0.016 m, blade chord at 70% of the blade's span, [m]
$d$	=	grid bar width, [m]
$D_{ext}$	=	additional contraction exit nozzle diameter, [-]
$D_p$	=	propeller diameter, [m]
$D_{wt}$	=	wind tunnel exit nozzle diameter, [m]
$f_a$	=	sampling frequency, [Hz]
$f_c$	=	band center frequency, [Hz]
$He$	=	$2\pi f c_{0.7}/c_\infty$ , chord-based Helmholtz number, [-]
$J$	=	$V_\infty/(n_s D_p)$ , advance ratio, [-]
$L_p$	=	sound pressure level relative to $p_{ref} = 20 \mu\text{Pa}$ , [dB]
$L_p^*$	=	sound pressure level scaled by relative dynamic pressure $q_r$ , [dB]
$L_{p,b}$	=	sound pressure level of 1/3-octave band centered around $f_c$ , [dB]
$M$	=	grid mesh width, [m]
$M_\infty$	=	$V_\infty/c_\infty$ , freestream Mach number, [-]
$M_{tip}$	=	$V_{tip}/c_\infty$ , tip Mach number, [-]
$n_s$	=	shaft rotational frequency, [Hz]
$p'$	=	vector of recorded acoustic pressure fluctuations, [Pa]
$q_r$	=	$0.5\rho_\infty V_r^2$ , relative flow dynamic pressure at 70% of the blade's span, [-]

\*Corresponding author, Postdoctoral researcher, Operations & Environment (O&E), l.n.quaroni@tudelft.nl

<sup>†</sup>Assistant professor, Flight Performance and Propulsion (FPP), t.sinnige@tudelft.nl

<sup>‡</sup>Assistant professor, Operations & Environment (O&E), r.merinomartinez@tudelft.nl

$q_\infty$	=	$0.5\rho_\infty V_\infty^2$ , dynamic pressure in the freestream, [-]
$r$	=	radial coordinate with origin at propeller's axis of rotation, [m]
$Re_{0.7}$	=	$c_{0.7}V_{0.7}/\nu_\infty$ , chord-based Reynolds number at 70% of the blade's span, [-]
$R_p$	=	propeller radius, [m]
$S_{pp}$	=	power spectrum of acoustic pressure fluctuations, [ $\text{Pa}^2/\text{Hz} - \text{Pa}^2$ ]
$S_{pp}^b$	=	broadband-only power spectrum of acoustic pressure fluctuations, [ $\text{Pa}^2/\text{Hz} - \text{Pa}^2$ ]
$St$	=	$fc_{0.7}/V_r$ , chord-based Stouhal number at 70% of the blade's span, [-]
$T$	=	propeller thrust, [N]
$T_C$	=	$T/(q_\infty A_p)$ , thrust coefficient, [-]
$v$	=	instantaneous streamwise velocity, [m/s]
$v_{rms}$	=	root mean square of instantaneous streamwise velocity, [m/s]
$V$	=	average streamwise velocity at hot-wire measurement point with propeller running, [m/s]
$V_\infty$	=	average wind tunnel streamwise velocity, [m/s]
$V_r$	=	$\sqrt{(\Omega_s \cdot 0.7R_p)^2 + V_\infty^2}$ , relative inflow velocity at 70% of the blade's span, [m/s]
$V_{tip}$	=	$\sqrt{(\Omega_s R_p)^2 + V_\infty^2}$ , relative inflow tip velocity, [m/s]
$V_{ref}$	=	average streamwise velocity at measurement point with propeller substituted by dummy spinner, [m/s]
$\beta$	=	$A_{flow}/A_{wt}$ , grid porosity, [-]
$\beta_{0.7}$	=	blade pitch angle at 70% of the blade's span, [ $^\circ$ ]
$\Lambda_x$	=	streamwise integral turbulence length scale, [m]
$\theta$	=	polar angle of directivity arc microphones, [ $^\circ$ ]
$\Phi_{vv}$	=	power spectrum of streamwise velocity fluctuations, [ $(\text{m/s})^2/\text{Hz}$ ]
$\chi$	=	$B\Omega_s\Lambda_x/V_\infty$ , haystacking parameter, [-]
$\nu_\infty$	=	air kinematic viscosity in the freestream, [ $\text{m}^2/\text{s}$ ]
$\rho_\infty$	=	air density in the freestream, [ $\text{kg}/\text{m}^3$ ]
$\Omega_s$	=	$2\pi n_s$ , shaft angular frequency, [rad/s]
$\omega_0$	=	angular non-dimensional frequency of Morlet wavelet function, [-]
<b>BLI</b>	=	<b>Boundary Layer Ingestion</b>
<b>BPF</b>	=	$n_s B$ , <b>Blade Passing Frequency</b> , [Hz]
<b>CR</b>	=	$A_{wt}/A_{ext}$ , <b>Contraction Ratio</b> , [-]
<b>CWT</b>	=	<b>Continuous Wavelet Transform</b>
<b>EA</b>	=	<b>Ensemble Averaging</b>
<b>HWA</b>	=	<b>Hot-Wire Anemometry</b>
<b>SMSB</b>	=	<b>Square Mesh Square Bar</b>
<b>TI</b>	=	$v_{rms}/V \cdot 100$ , <b>streamwise Turbulence Intensity</b> , [%]
<b>TIN</b>	=	<b>Turbulence Ingestion Noise</b>
<b>TSA</b>	=	<b>Time Synchronous Averaging</b>
<b>UAV</b>	=	<b>Unmanned Aerial Vehicle</b>

## I. Introduction

The ubiquity of drones and the rise in non-conventional aircraft architectures (i.e. distributed electric propulsion, planar/axisymmetric boundary layer ingestion systems [1, 2]) has put the topic of propeller noise back at the center stage in recent years, after a period of relative quiet in the scientific community. Propellers may offer a more efficient alternative to traditional propulsive technologies (e.g. turbofan engines [3]) or, as in the case of Unmanned Aerial Vehicles (UAVs) such as drones, the only viable solution for the flexibility required in their operation [4]. The large number of possible arrangements, however, may involve the positioning of propellers in configurations in which strong flow interactions with the airframe are present. Such types of installation effects may lead to greatly increased noise emissions, which are challenging to predict and, therefore, to avoid [5]. The greater knowledge of the adverse health effects posed by noise exposure and the development of more advanced sound metrics taking into account the specificity of human sound perception adds another layer of complexity to the issue [6–8].

A common installation effect in most non-conventional propeller configurations is the production of a non-uniform and non-homogeneous turbulent inflow velocity field to the rotor disk, e.g. boundary layer ingestion (BLI) systems and frame-wake interaction in drones [9, 10]. Whilst actively sought in certain configurations due to the benefits in propulsive efficiency, the ingestion of highly-distorted turbulent flows leads to an overall increase in noise levels [11]. Spatial non-uniformity of the inflow velocity field to the propeller mainly acts on the amplification of tonal noise due to the propeller blades experiencing a periodic change in their local sectional angle of attack during their rotation around the propeller axis [12]. This causes the presence of harmonically fluctuating lift and drag forces, which in turn translate into a highly tonal acoustic pressure field at the observer’s position, with its frequency content distributed between the Blade Passing Frequency (BPF) and its harmonics [13, 14]. Turbulence ingestion, on the other hand, is predominantly linked to an increase in broadband noise. The vortical structures present in a turbulent flow cause a rise in the pressure fluctuations at the blade’s surface due to their direct impingement on the blade’s leading edge [15]. This increase may not be limited to the blade’s leading edge region, however [16]. The scattering of such pressure fluctuations by the blade’s trailing edge (e.g. [17]) may then be a further cause of the amplification in the broadband noise production from turbulence-ingesting propellers. The influence of turbulence ingestion is, however, not limited only to a general increase in broadband noise levels. If the eddies present in the flow are ‘stretched’ long enough, the same structure can interact with multiple blades. The result is the grouping of broadband noise into ‘humps’ (resembling ‘haystacks’, hence the name of the phenomenon: ‘haystacking’) around the BPF and its harmonics [12, 18, 19]. A criterion for this to occur is that the ‘haystacking parameter’  $\chi = B\Omega_s\Lambda_x/V_\infty \gg 1$  [14]. This parameter provides a measure of the number of times that the largest vortical structures present in the flow are ‘chopped’ by the propeller’s blades, and its value is, therefore, dependent on the integral length scale of the ingested turbulence.

Additional noise generation mechanisms are present when dealing with the typical dimensions of scaled-down propeller models employed in wind tunnels or UAVs. The small propeller blade chords may lead to laminar separation bubbles due to the relatively low chord-based Reynolds numbers involved, influencing both the blade loading distribution and the associated noise emissions [20]. Furthermore, the electric motors typically employed in small-scale propellers may heavily contaminate the acoustic measurements with noise contributions rich in tonal content over a large frequency range [21]. It is worth mentioning that the issue of motor noise is present at larger scales and for different types of motors as well, such as the exhaust tones produced by reciprocating engines [22].

From the above discussion, it is clear that a separation of the noise generated by propellers into its more fundamental components, i.e. deterministic (tonal) and stochastic (broadband), may be of help in both shedding more light on the physical mechanisms at play and in correctly interpreting experimental results. A review of the most widely used techniques in the context of propeller noise separation was provided by Bonomo *et al.* in [23]. The relatively straightforward Time Synchronous Averaging (TSA) method, also known as ‘Ensemble Averaging’ (EA), was found to be the most effective at separating tonal and broadband components of propeller noise signals if the operation of the propeller can be considered relatively steady in time. The method is based on the subdivision of the signal into segments corresponding to a full shaft revolution using the one-per-revolution signal provided by an optical encoder or tachometer. Averaging of these segments over time then allows the retrieval of the deterministic component. In order to remove the need for a constant shaft frequency or for tachometer rotational data, the cross-correlation method proposed by Sree was also shown to provide satisfactory results, especially regarding the separation of the broadband component [24, 25]. The two techniques can help in identifying the general acoustic features of propeller noise generation, providing easy-to-use time-independent metrics (i.e. Overall Sound Pressure Levels (OSPLs), directivity patterns, etc.). If, however, the phenomenon at hand is inherently unsteady, as is the case for turbulence-ingesting propellers, an analysis considering the time-dependent behavior of the signal’s statistics might prove beneficial for a better understanding of the physical phenomena at play. The use of the continuous wavelet transform (CWT), alongside the more traditional Fourier one, shows promising results in this respect [26, 27]. By construction, the wavelet transform is well suited for the identification of intermittent phenomena, such as the impulsive noise signatures of turbulent eddies impinging on the propeller’s blades in BLI systems [28].

The present paper reports the results of an experimental campaign on a model-propeller ingesting a grid-generated turbulence field. In particular, the focus is on the determination of the time-averaged features of the far-field acoustic signal produced by the propeller through the phase-averaging and phase-matching techniques mentioned above. An analysis of the additional time-dependent information obtained through the application of the wavelet transform method is also included. The overarching aim is to provide greater insight into the acoustic consequences of turbulence ingestion

by propellers, in an effort to mimic part of the installation effects found in more complex ‘real-world’ applications. The manuscript is structured as follows. Section II presents the experimental setup and measurement techniques employed. Section III instead provides a description of the signal processing methods briefly mentioned above. Section IV discusses the main results, whereas section V draws the conclusions.

## II. Experimental setup and methods

The experimental campaign was performed at the anechoic open-jet wind tunnel facility, known as ‘A-Tunnel’, at Delft University of Technology. A characterization of the facility can be found in Merino-Martínez *et al.* [29]. The same setup as described in Quaroni *et al.* [30] was employed (Figure 1). The circular outlet of the wind tunnel (exit diameter  $D_{wt}$  of 600 mm) located on the floor of the facility has a contraction ratio (CR) of 15.

The setup features a steel six-bladed propeller of diameter  $D_p$  equal to 203.2 mm (8") with a manually adjustable blade pitch angle. For the present analysis, the blade pitch angle at 70% of the span is set to  $\beta_{0.7} = 30^\circ$ . The propeller is mounted at a distance of  $0.6 D_{ext}$  from the exit plane of a contracting axisymmetric nozzle. This propeller has been the subject of a number of publications; for its geometry, including spinner and nacelle dimensions, the reader is referred to [31]. The aerodynamic performance of the propeller is provided in [9].

Inflow turbulence was generated through the application of 5-mm-thick square-mesh and square-bar (SMSB) grids positioned at the main circular outlet of the wind tunnel. An additional axisymmetric contraction of inlet diameter  $D_{wt}$  equal to 600 mm (23.2") and exit diameter  $D_{ext}$  equal to 420 mm (16.5") (i.e. with  $CR = A_{wt}/A_{ext} \approx 2$ ) is placed downstream of the grids for improving the isotropy of the generated turbulence and reducing the self-noise of the grids [32, 33]. The use of different mesh sizes with a constant porosity  $\beta = A_{flow}/A_{wt} = 0.64$  allowed for various combinations of streamwise turbulence intensity levels  $TI$  and turbulence integral length scales  $\Lambda_x$  to be obtained. Table 1 reports the main dimensions of the grids. Acoustic absorbent materials (melamine and pyramidal polyurethane foam panels) were positioned over all exposed surfaces within the anechoic plenum to reduce acoustic reflections, including a 10-mm-thick cylindrical insert with a sloped leading edge covering the inner walls of the end (cylindrical) segment of the axisymmetric contraction. Additionally, 20-mm-thick melamine foam panels were water-jet cut and glued onto the downstream side of the turbulence-producing grids in order to reduce secondary reflections, suppress spurious tones, and reduce the grids’ self-noise, as suggested in [34]. A second contribution by some of the authors of this paper is focused on this particular aspect, and the reader is referred to it for more details [35].

**Table 1** Porosity  $\beta$ , bar width  $d$ , and mesh length  $M$  of the turbulence-producing grids (see Figure 1).

Grid	$\beta$	$d$	$M$
[-]	[-]	[mm]	[mm]
A	0.64	7	35
B	0.64	10	50
C	0.64	12	60

### A. Measurement techniques

The streamwise inflow velocity field to the propeller was measured through hot-wire anemometry (HWA) at discrete positions along a single radial line, from  $r/R_p = 0.3$  to  $r/R_p = 1.1$ , with steps between 5 to 10 mm at a distance of  $0.15R_p$  upstream of the propeller’s disk. This allowed the statistics of the streamwise turbulence being ingested by the propeller to be retrieved. A 7-hole pressure probe was also employed to quantify the propeller loading and obtain a measure of the thrust produced by the propeller. The details of this are not included in the present analysis but can be found in Quaroni *et al.* [35]. The acoustic measurements were performed through a planar phased array containing 63 free-field G.R.A.S. 40PH microphones and a directivity arc containing 8 G.R.A.S. 46BE high-frequency microphones spanning an emission angle range of  $70^\circ$  from  $\vartheta = 70^\circ$  to  $140^\circ$  with the  $90^\circ$  plane corresponding to the rotor disk plane and the upstream direction at  $\vartheta = 0^\circ$ . All polar angles and pressure amplitudes have been corrected for flow convection effects using the method proposed by Amiet [36]. Both arrays were positioned at a distance of 1.3 m ( $\approx 6.5 D_p$ ) from

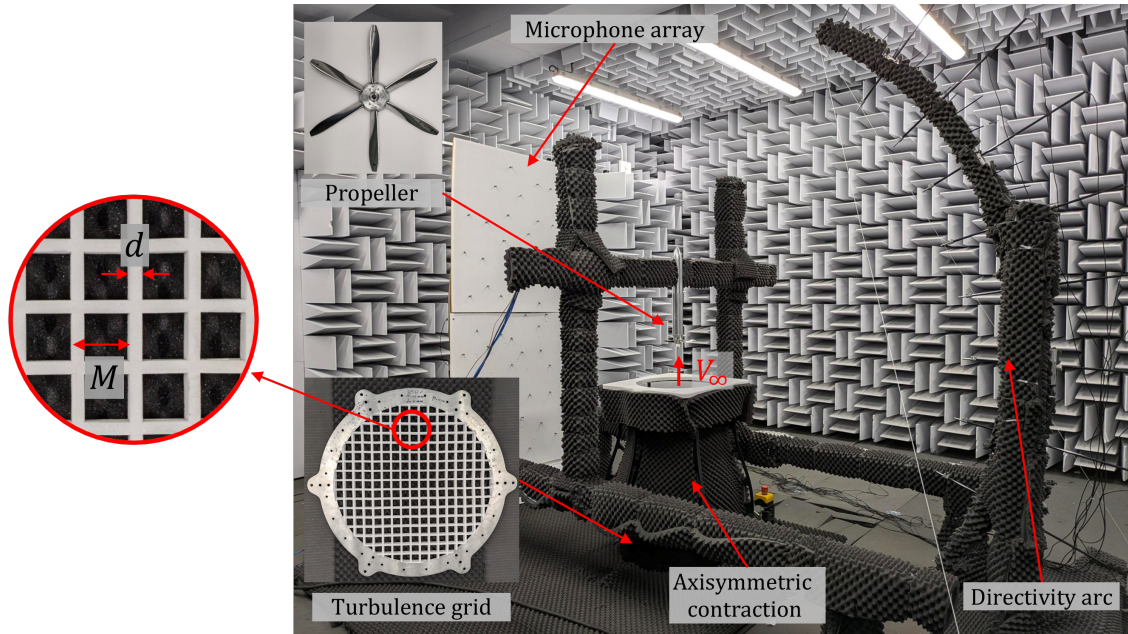


**Fig. 1** Overview of the experimental setup at the anechoic open-jet wind tunnel ‘A-Tunnel’ at Delft University of Technology during the acoustic tests. The highlighted area shows the grid dimensions reported in Table 1 (Grid A taken here as an example). Notice the melamine foam coating on both the nozzle flange and the grids.

the propeller’s axis, with the directivity arc centered on the propeller’s rotation center. A one-per-revolution (1p) optical encoder was also installed and its signal was acquired synchronously with both the hot-wire and microphone data at a sampling frequency  $f_a = 51200$  Hz to allow for the application of TSA separation techniques. The hot-wire signal was bandpass filtered between 30 Hz and 15000 Hz to reduce the influence of spurious low/high frequency noise due to the wind tunnel operation and acquisition system, respectively. The total recording time was set to  $T_{rec} = 60$  s for the acoustic measurements (limited to  $T_{rec} = 45$  s for the hot-wire measurements), producing  $N = T_{rec} f_a = 3.072 \cdot 10^6$  samples per microphone per test case. This recording time corresponds to approximately 10,000 rotations acquired per operating condition.

## B. Test matrix

The propeller was tested under the operating conditions reported in Table 2. For the definition of each quantity, the reader is referred to the List of Symbols. The operating points were chosen based on a trade-off between hardware limitations (maximum torque of the BLDC electric motor), similarity with full-scale cases (tip Mach numbers as high as possible, up to 0.35 in the present case), and avoidance of stalling. However, due to the small dimensions of the propeller, the chord-based Reynolds number  $Re_{0.7}$  never exceeds the threshold value of  $10^5$ , making laminar separation bubbles likely to occur [37].

## III. Signal processing methods

The two separation methods for tonal/broadband noise mentioned in section I, i.e. the ‘Ensemble Averaging’ method (EA) and the signal cross-correlation algorithm proposed by Sree [24, 25] are described in this section. Moreover, the concept of the continuous wavelet transform (CWT) is also explained.

### A. Ensemble Averaging (EA)

Any deterministic noise signal aerodynamically produced by a propeller in a steady flow will repeat itself with a period equal (at least) to the time required for one of its blades to perform a full rotation about the propeller’s axis, i.e. the shaft period  $T_s$ . Assuming a constant rotational frequency (i.e.  $n_s = 1/T_s = \text{const.}$ ) and an integer number of samples per revolution  $N_{spr}$ , it is possible to subdivide the time history of the acoustic pressure fluctuations  $p'$  into  $N_{rev}$  (number

**Table 2 Propeller operating conditions investigated in the present study.**

$\beta_{0.7}$ [deg]	Grids [-]	$V_\infty$ [m/s]	$M_\infty$ [-]	$Re_{0.7}$ [-]	$M_{tip}$ [-]	$J$ [-]	BPF [Hz]	$T_C$ [-]
30	off, A, B, C	25	0.073	$7.6 \cdot 10^4$	0.300	0.794	930	0.939
				$8.1 \cdot 10^4$	0.325	0.730	1013	1.179
		30	0.088	$7.7 \cdot 10^4$	0.300	0.967	917	0.624
				$8.2 \cdot 10^4$	0.325	0.886	1000	0.815
				$8.8 \cdot 10^4$	0.350	0.818	1083	0.996

of full revolutions) segments of length  $N_{spr}$  denoted as  $\mathbf{p}'_n$ . This vector will be the sum of a deterministic (tonal) part  $\bar{\mathbf{p}}'$  repeating at every rotation and of a random (broadband) component  $\mathbf{p}'_{bb,n}$ :

$$\mathbf{p}'_n = \bar{\mathbf{p}}' + \mathbf{p}'_{bb,n} \quad (1)$$

If  $N_{rev}$  is sufficiently high, any random component  $\mathbf{p}'_{bb,n}$  present in each realization  $\mathbf{p}'_n$  will average out to zero, leading to an estimate of the deterministic component  $\bar{\mathbf{p}}'$ :

$$\frac{1}{N_{rev}} \sum_{n=1}^{N_{rev}} \mathbf{p}'_n = \frac{1}{N_{rev}} \sum_{n=1}^{N_{rev}} \bar{\mathbf{p}}' + \left( \frac{1}{N_{rev}} \sum_{n=1}^{N_{rev}} \mathbf{p}'_{bb,n} \right) \approx \bar{\mathbf{p}}' \quad (2)$$

$\rightarrow 0 \text{ if } N_{rev} \rightarrow +\infty$

The shaft frequency  $n_s$  is, however, never perfectly constant in real-world applications. To account for the small (and random) variations usually present, Bonomo *et al.* [23] suggested the use of the ‘order tracking’ method discussed in [38]. In practice, each realization  $\mathbf{p}'_n$  is resampled in terms of  $N_\theta$  shaft angle positions  $\theta^* \in [0, 2\pi]$ , assuming that the shaft rotational velocity remains constant during the  $n$ -th rotation of duration  $T_{s,n}$ . The identification of the segment duration is performed through the use of the one-per-revolution signal pulse generated by the optical encoder. Applying (2), therefore, yields the deterministic component  $\bar{\mathbf{p}}'(\theta^*)$ . Appending both  $\mathbf{p}'_n(\theta^*)$  and  $\bar{\mathbf{p}}'(\theta^*)$  in single vectors  $\mathbf{p}'_{res}(\theta)$  and  $\bar{\mathbf{p}}'_{res}(\theta)$ , with  $\theta \in [0, 2\pi N_{rev}]$ , allows to retrieve the random (broadband) component  $\mathbf{p}'_{bb}(\theta)$  by subtracting the latter from the former. Since the new vectors express the acoustic pressure variation in the shaft-angle domain rather than in time, any Fourier analysis will lead to the results being expressed as fractions of the shaft frequency, i.e. frequencies normalized by  $n_s$ . It is worth highlighting the fact that this method is only able to extract deterministic signals of frequency equal to the shaft frequency  $n_s$  and its multiples, including, therefore, the BPF and its harmonics.

### B. Sree’s cross-correlation algorithm

The method was originally developed for counter-rotating open rotors displaying random phase changes in the data record and lacking synchronization [24]. Its main advantage is that it does not require encoder data and can, therefore, deal with deterministic components in the signal that are not necessarily related to the shaft frequency  $n_s$ . The idea behind this method is to account for the dominant phase shift  $\Delta\tau$  between consecutive segments  $\mathbf{p}'_n$  and  $\mathbf{p}'_{n+1}$  of equal length  $N_s$  of the acoustic pressure fluctuations observations vector  $\mathbf{p}'$ . This can be done by computing the sample shift  $r_s = f_a \Delta\tau$  corresponding to the maximum value of the cross-correlation coefficient  $\hat{R}_{\mathbf{p}'_n, \mathbf{p}'_{n+1}}$  between the two time series, that is, if  $r > 0$ :

$$\left\{ \Delta\tau | \hat{R}_{\mathbf{p}'_n, \mathbf{p}'_{n+1}}(r_s = f_a \Delta\tau) = \frac{\sum_{k=0}^{N_s - r_s - 1} (x_{k+r_s})(y_k^*)}{\sqrt{\left( \sum_{k=0}^{N_s - 1} x_k^2 \right) \left( \sum_{k=0}^{N_s - 1} y_k^2 \right)}} = \max \left( \hat{R}_{\mathbf{p}'_n, \mathbf{p}'_{n+1}} \right) \right\}, \quad (3)$$

where the notation  $x_{k+r_s}$  indicates the  $(k+r_s)$ -th component of the vector  $\mathbf{p}'_n$  and  $y_k^*$  is the complex-conjugate of the  $k$ -th component of the vector  $\mathbf{p}'_{n+1}$ . If  $r_s < 0$ , the signal  $\mathbf{p}'_n$  ‘follows’  $\mathbf{p}'_{n+1}$  and the relationship  $\hat{R}_{\mathbf{p}'_n, \mathbf{p}'_{n+1}}(r_s) = \hat{R}_{\mathbf{p}'_{n+1}, \mathbf{p}'_n}^*(-r_s)$  is valid. If the random component is assumed to be stationary, i.e. its mean and the root-mean-square are time-invariant,

subtracting vector  $\mathbf{p}'_{n+1}$  to the shifted  $\mathbf{p}'_n(r_s)$  and dividing it by  $\sqrt{2}$  will yield the broadband component  $\mathbf{p}'_{bb,N}$  for the  $N = (n + 1)/2$ -th segment pair. Appending  $\mathbf{p}'_{bb,N}$  then allows for the reconstruction of a ‘pseudo’ time series of the broadband signal  $\mathbf{p}'_{bb}$  of half the length of the original  $\mathbf{p}'$  data record. While not strictly necessary, choosing a number of samples  $N_s$  for the vector segments  $\mathbf{p}'_n$  equal to the (rounded to integer) number of samples per revolution  $N_{spr}$  is recommended, since it improves the overall performance of the method [25].

### C. Continuous Wavelet Transform (CWT)

For a general introduction to the subject, the reader is referred to the reference book by Addison [39]. The present subsection is limited to the case of the continuous wavelet transform (CWT) and draws from the introductory paper by Torrence & Compo [40]. The CWT of a continuous signal  $x(t)$  is defined as:

$$w(s, \tau) = \int_{-\infty}^{+\infty} x(t) \psi^* \left( \frac{t - \tau}{s} \right) dt \quad (4)$$

where  $s$  is denoted as the ‘scale’ of the transform,  $\tau$  is a time-shifting parameter,  $\psi$  is the wavelet function, and  $*$  denotes complex conjugation. Many different choices for  $\psi$  are available, but the core concept is that of short oscillatory pulses which can be shifted, stretched, or contracted in time, all the while maintaining the same number of meaningful oscillations. A widely used wavelet function is the complex Morlet wavelet, defined as:

$$\psi_0(t, s, \tau) = \pi^{-1/4} \exp \left( i \frac{\omega_0}{s} (t - \tau) \right) \exp \left( - \frac{(t - \tau)^2}{2s^2} \right) \quad (5)$$

where the zero subscript indicates the unscaled wavelet (also known as ‘mother wavelet’, being the scaled wavelet  $\psi = \psi_0/\sqrt{s}$ ) and  $\omega_0 = 2\pi f_0$ , with  $f_0$  the wavelet’s central non-dimensional frequency. It can be seen how (5) represents a harmonic wave modulated by a Gaussian curve around the time instant  $(t - \tau)$  and with standard deviation equal to the scale  $s$ . Increasing the scale has the effect of decreasing the wavelet’s effective frequency  $\omega_0/s$ , ‘stretching’ the function in time. Equation (4) corresponds to the mathematical operation of convoluting the wavelet function  $\psi$  with the signal  $x(t)$ . An alternative form of (5) is given in the frequency domain through the convolution theorem [41]:

$$w(s, \tau) = \int_{-\infty}^{\infty} \hat{X}(f) \hat{\Psi}(s, f) e^{2\pi i f(t-\tau)} df \quad (6)$$

where the hat symbol and the capital letter indicate the Fourier transform of the relative quantity. It can be shown that  $\hat{\Psi}(s, f) = \sqrt{s} \exp(-2\pi i f \tau) \hat{\Psi}_0(s, f)$ , with  $\hat{\Psi}_0(s, f)$  having the following analytical expression for the Morlet wavelet:

$$\hat{\Psi}_0(s, f) = \pi^{-1/4} \exp \left( - \frac{4\pi^2 (f - f_0/s)^2}{2(1/s^2)} \right) \quad (7)$$

The operation in (6) essentially corresponds to filtering  $x(t)$  with a Gaussian-like filter centered at  $f = f_0/s$  and characterized by a standard deviation equal to  $1/s$ . The conversion of the wavelet scale  $s$  to the Fourier frequency  $f$  in the case of a Morlet complex wavelet is given by the formula [40]:

$$f = \frac{\omega_0^2 + \sqrt{2 + \omega_0^2}}{8\pi^2 s} \quad (8)$$

In the case of a discrete signal  $\mathbf{x}$  of  $N$  samples, (6) is written as:

$$w_n(s) = \sum_{k=0}^{N-1} \hat{X}_k \hat{\Psi}(s\omega_k)^* e^{2\pi i kn/N} \quad (9)$$

where  $\hat{X}_k$  is the  $k$ -th component of the Discrete Fourier Transform (DFT) of  $\mathbf{x}$ , the only limitation on  $s$  being that the relative Fourier frequency  $f \leq f_a/2$ , with  $f$  computed through (8). Compared to the classical Short-Time Fourier Transform (STFT), the CWT has the advantage of being able to ‘adjust’ its time window based on the frequency being considered, with larger time windows for larger scales (i.e. lower frequencies) and vice versa at smaller scales (i.e. larger frequencies). This leads to a larger frequency resolution at smaller scales and a larger time resolution at smaller scales, the downside of course being a smaller time resolution at larger scales and a smaller frequency resolution at smaller scales. It has to be noted, however, that high-frequency phenomena tend to occur in short-lived bursts (e.g. an imploding

bubble in cavitation phenomena) while low-frequency behaviours are usually more characteristic of longer time-scales, therefore reducing the need for large time resolutions (e.g. structural oscillations in suspended bridges).

## IV. Results

The present section is divided into two parts. In particular, IV.A presents a description of the propeller inflow field as obtained using the single-wire hot-wire probe installed  $0.15R_p$  upstream of the propeller's plane. Then, IV.B reports the an analysis of the turbulence ingestion noise in the acoustic far-field.

### A. Inflow turbulence characteristics

The inflow turbulence characteristics were measured through HWA to quantify the temporal variations in propeller inflow due to the grids. Hot-wire probes in close proximity to a rotating propeller can however be affected by the periodic passage of the blades and the associated induced velocity field. The amplitude of the velocity fluctuations associated with this phenomenon may far exceed those of the turbulent inflow, making it difficult to properly characterize it. This in fact translates into the presence of large peaks at the BPF and its harmonics in the otherwise broadband spectrum of the velocity fluctuations. Go *et al.* [42] employed a comb filter to remove such tones, resulting, however, in the removal of broadband energy from the original spectrum, especially at higher harmonics of the BPF. Figure 2 reports the power spectrum of the streamwise velocity signal at  $0.15R_p$  upstream of the propeller's disk and at 70% of the blade's span for the turbulence grid C ( $M_\infty = 0.088$ ,  $M_{tip} = 0.325$ ). In particular, both the cases of the original, unfiltered signal and that of the same signal filtered through the EA and Sree methods of III are considered. It can be seen how the EA method is able to effectively suppress the near-field tones present in the original signal at the BPF and its harmonics. Sree's method also performs satisfactorily, even though a small residual peak is still present at the BPF and some energy is added to the spectrum at low frequencies ( $f/BPF < 0.1$ ). This last point was also remarked by Bonomo *et al.* [23].

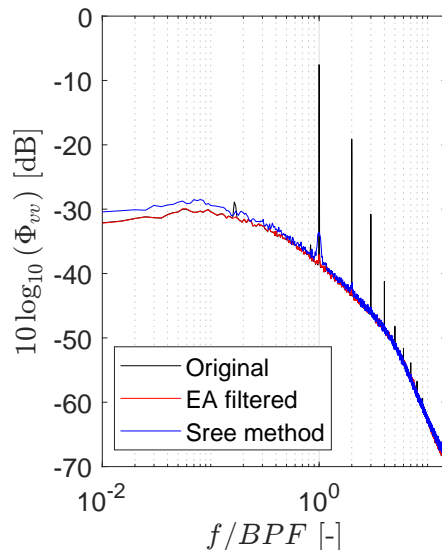


**Fig. 2 Power spectra of original and filtered streamwise velocity signal at  $0.15R_p$  upstream of the propeller's disk and at 70% of the blade's span ( $M_\infty = 0.088$ ,  $M_{tip} = 0.325$ , grid C). Frequency resolution  $\Delta f = 5$  Hz.**

Figure 3 shows the evolution of the broadband power spectra along the radial direction for the three grids tested in the present work. The better-performing EA-filtering method was used. The spectra are relative to  $M_{tip} = 0.325$  and  $M_\infty = 0.088$ , but similar results were obtained for the other operating conditions. It can be noticed that the overall shape of the spectra remains constant for all of the radial stations considered. However, differences in amplitude arise for Strouhal numbers  $St = fc_{0.7}/V_\infty \lesssim 0.5$ , with outboard spectra showing larger amplitudes than those at more inboard positions. This difference is increasingly more important for decreasing frequencies and has the largest gradient around  $r/R_p \approx 0.7$ . Figure 4 shows the radial trends of the temporal average point-wise velocity  $V$ , the root mean square of the streamwise velocity fluctuations  $v_{rms}$ , and the longitudinal integral length scale  $\Lambda_x$  for the same test conditions as in Figure 3. This last quantity is computed by integrating the autocorrelation of the velocity signal until the first zero

crossing [42]. The velocity  $V$  is normalized by the reference velocity  $V_{ref}$  measured at the same radial station with the propeller replaced by a dummy spinner (referred to as ‘propeller-off’ condition in the following). This allows for taking into account the disturbance to the inflow field caused by the presence of the nacelle. The root mean square of the velocity fluctuations ( $v_{rms}$ ) is instead normalized by the average velocity  $V$ , which, therefore, includes the added velocity due to the propeller’s operation. It can be seen how the average inflow velocity distribution is only marginally affected by the grids, while its maximum lies at around 70% of the blade’s span, in line with the radial station expected to be responsible for the largest lift production for this propeller (e.g. [9]). The normalized  $v_{rms}$  and the longitudinal integral length scale  $\Lambda_x$  instead follow an opposing trend with respect to  $V$ , with a decrease in amplitude for inboard stations.

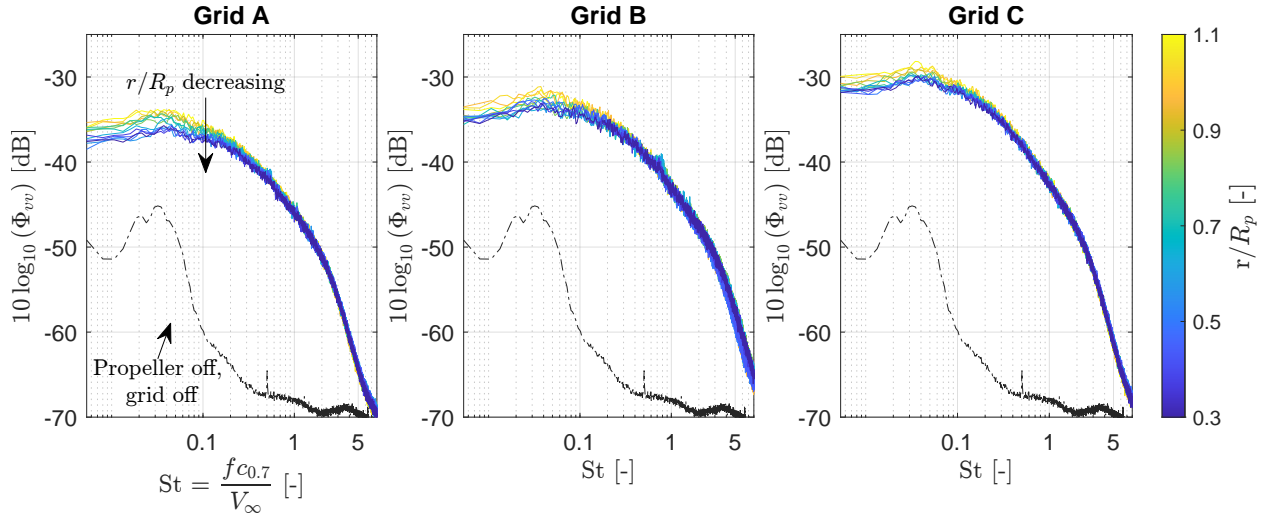


**Fig. 3** Power spectra of the broadband component of the streamwise velocity along the radial line of measurement for the three grids ( $M_\infty = 0.088$ ,  $M_{tip} = 0.325$ ,  $0.15R_p$  upstream of the propeller’s disk). Frequency resolution  $\Delta f = 5$  Hz.

Figure 5 shows a comparison of the radial trends of  $v_{rms}$  and  $\Lambda_x$  between the ‘propeller-off’ and the ‘propeller-on’ conditions for the three turbulence grids. The streamwise velocity fluctuations are now normalized by the reference wind tunnel free stream velocity  $V_\infty$  to aid in the comparison. Furthermore,  $v_{rms}$  scales with  $V_\infty$  for the cases with grid-generated turbulence [43]. It can be seen how both  $\Lambda_x$  and  $v_{rms}/V_\infty$  show an inboard decrease caused by the presence of the propeller. The latter in particular is evidence that the decreasing trend observed in Figure 4 (center) is due not only to normalization by the average pointwise velocity  $V$  but also to a decrease in the  $v_{rms}$  itself. This is of course a consequence of the decrease in energy observed at lower frequencies for the more inboard stations (Figure 3). Table 3 reports the value of the hystacking parameter  $\chi$  for all grids and all the considered propeller operative conditions. Mind that the ‘propeller off’ value of the longitudinal integral lengthscale has been used in its computation.

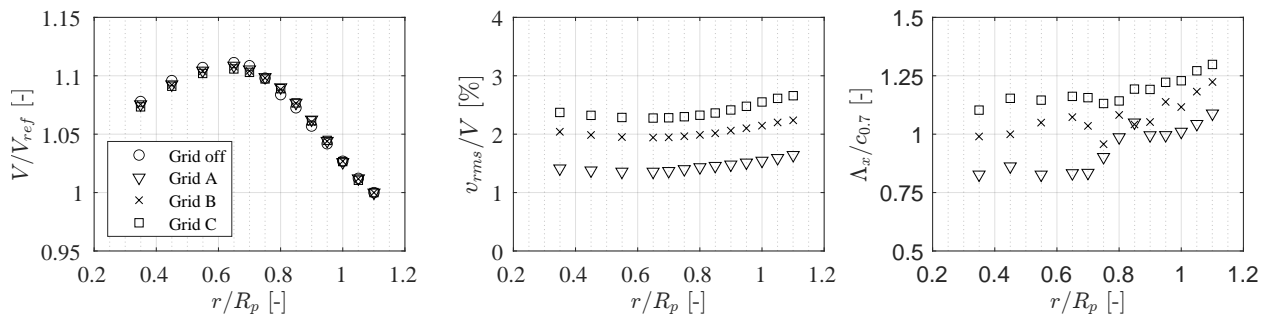


**Fig. 4** Radial trends of (left) average streamwise velocity  $V$  (normalized by the ‘propeller-off’ velocity  $V_{ref}$ ), (center) root mean square of velocity fluctuations  $v_{rms}$  (normalized by the average streamwise velocity  $V$ ), and (right) longitudinal integral length scale  $\Lambda_x$  (normalized by the chord at 70% of the blade span) for all the test grids ( $M_\infty = 0.088$ ,  $M_{tip} = 0.325$ ,  $0.15R_p$  upstream of the propeller’s disk).

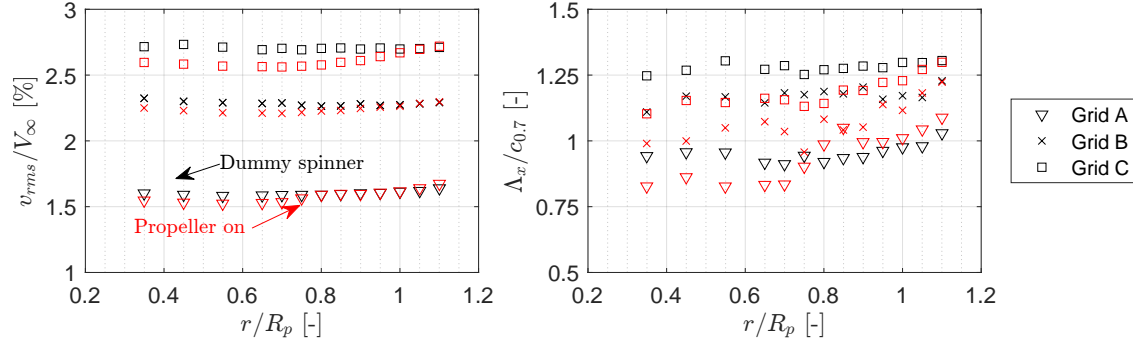


**Fig. 5** Radial trends of (left) root mean square of velocity fluctuations  $v_{rms}$  (normalized by the wind tunnel freestream velocity  $V_\infty$ ) and (right) longitudinal integral length scale  $\Lambda_x$  for all the test grids with (in red) and without (in black) the propeller running ( $M_\infty = 0.088$ ,  $M_{tip} = 0.325$ ,  $0.15R_p$  upstream of the propeller's disk).

**Table 3** Haystacking parameter  $\chi$  for propeller operative conditions.

$M_\infty$ [-]	0.074		0.088			Grid
$M_{tip}$ [-]	0.300	0.325	0.300	0.325	0.350	
$\chi$ [-]	2.120	2.323	1.689	1.921	2.041	A
	2.741	2.987	2.192	2.513	2.725	B
	3.031	3.241	2.389	2.712	2.881	C

## B. Acoustic emissions

The present subsection reports the results obtained by the application of the tonal/broadband noise separation techniques discussed in III.A and III.B to the data from the experimental campaign outlined in II, showing the usefulness of these techniques in obtaining insights on turbulence ingestion noise (TIN) from propellers. Furthermore, IV.B.3 discusses the time-frequency domain analysis of the same data through the use of the CWT introduced in III.C.

### 1. Determination of tonal and broadband components

The case of the propeller rotating with  $M_{tip} = 0.325$  and  $M_\infty = 0.073$  under the inflow produced by the coarsest grid (C) is considered here. This corresponds to the case with the largest value of the ‘haystacking parameter’  $\chi$  (Table 3) based on the turbulence characteristics obtained with the ‘propeller-off’ measurements (see section IV.A). The deterministic acoustic signature  $\bar{p}'$  of the propeller as recorded by a microphone in the propeller's rotation plane ( $\theta = 90^\circ$ ) and computed using the phase-averaging (EA) method discussed in section III.A is reported in Figure 6, together with 100 realizations of  $p'_n$  for visualization purposes (the deterministic component was computed using the complete time series). As expected, the deterministic part of the signal displays a main periodicity linked to the BPF, as shown by the six main peaks and troughs evident during the rotational period  $T_r$ . The contribution of the random fluctuations is also clear, with total acoustic pressure amplitudes more than doubled with respect to the phase-averaged deterministic part. The same information is clearly visualized in the frequency domain. Figure 7 reports the sound pressure level  $L_p$  of the raw acoustic pressure signal, the tonal contribution related to the shaft frequency, and the broadband component for the same operating conditions. The sound pressure level is computed as:

$$L_p(f) = 10 \log_{10} \left( \frac{S_{pp}(f) \Delta f}{p_{ref}^2} \right) \quad (10)$$

where  $S_{pp}$  is the power spectrum of the acoustic pressure fluctuations at the frequency  $f$ ,  $\Delta f$  is the frequency resolution of the spectrum, and  $p_{ref} = 20 \mu\text{Pa}$  is the reference acoustic pressure. The frequency axis has been non-dimensionalized by the BPF. In particular, the deterministic component was obtained by performing a Fourier analysis of the signal

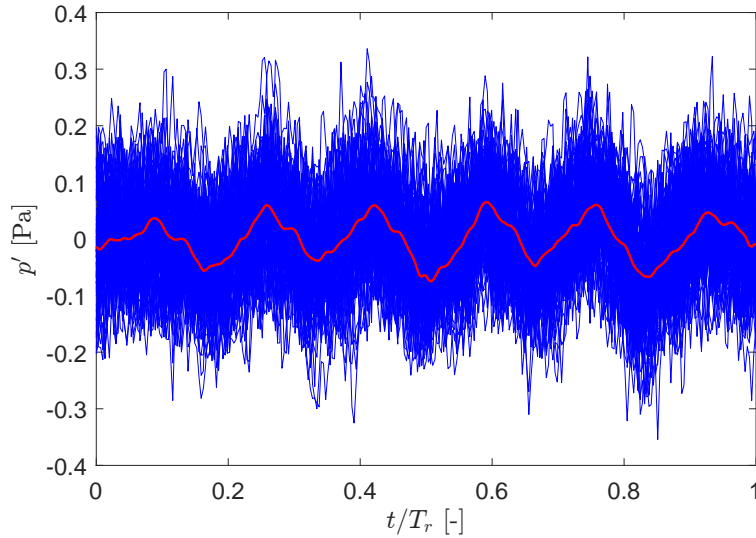


**Fig. 6** Deterministic acoustic signature  $p'_{res}$  computed through EA algorithm (in red) superposed to 100 different realizations of  $p'_n$  (in blue) over a rotation period  $T_s$  for the case of grid C turbulence ingestion,  $M_{tip} = 0.325$  and  $M_\infty = 0.073$  for a microphone in the propeller's plane ( $\vartheta = 90^\circ$ ).

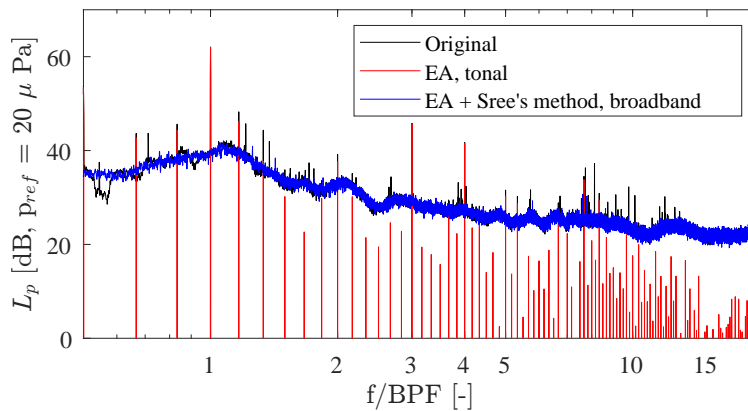


**Fig. 7** Sound pressure level ( $L_p$ ) of the raw signal (black), tonal component as computed through EA (red), and broadband component as computed through EA and Sree's cross-correlation method (blue). Operating conditions and microphone position same as the data reported in Figure 6 ( $\Delta f \approx 0.83$  Hz).

$\bar{p}'_{res}$  obtained by appending the deterministic acoustic signature shown in Figure 6 so that its length was equal to the raw data record  $p'$ . The broadband component  $p'_{bb}$  was retrieved by first subtracting  $\bar{p}'_{res}$  from  $p'$  and then applying Sree's cross-correlation algorithm to the result. It can be seen that the deterministic component obtained through the application of (2) only contains tones that are related to the shaft rotational frequency  $n_s$ . Any other coherent components that may be present due to mechanisms unrelated to the shaft rotation (e.g. vortex shedding, additional electric motor noise) are, therefore, still contained in the first 'broadband' signal estimate. The application of Sree's cross-correlation method on this first estimate of the random component will, therefore, suppress the most dominant remaining coherent noise sources and produce a better estimate of the actual broadband spectrum. The downside of this approach is that the length of the signal available for analysis is then halved, and, therefore, a lower number of averages can be applied in the computation of the Fourier transform. The benefit is a 'cleaner' estimate of broadband noise metrics, which might be otherwise sensitive to the presence of relatively high peaks due to residual tones. This approach (combination of EA and Sree's methods) is used in the following analysis of turbulence ingestion noise.

## 2. Analysis of turbulence ingestion noise

Turbulence ingestion noise is an inherently broadband phenomenon. Therefore, it follows that the application of separation methods of tonal/broadband noise components is particularly interesting in the analysis of its characteristics. Furthermore, this allows to make some considerations on its scaling with relevant parameters, as discussed in the following. Figure 8 shows the sound pressure level spectra  $L_p$  (frequency  $f$  not normalized) of the broadband component for a microphone located at  $\vartheta = 140^\circ$  for all the propeller operating conditions considered (see Table 2). The comparison is limited to the coarsest grid (C), but similar trends were obtained for the other grids. The microphone position is chosen to highlight the presence of any haystacking, if present, as the phenomenon is the most pronounced for polar positions approaching the propeller axis, downstream of the propeller disk (i.e.  $\vartheta = 180^\circ$ ). The most visible feature is the presence of a series of spectral undulations for all the cases considered. These ‘bumps’ are only weakly dependent on either  $V_\infty$  or  $M_{tip}$ . On the contrary, a direct proportionality of  $L_p$  with these same two parameters is clearly present.

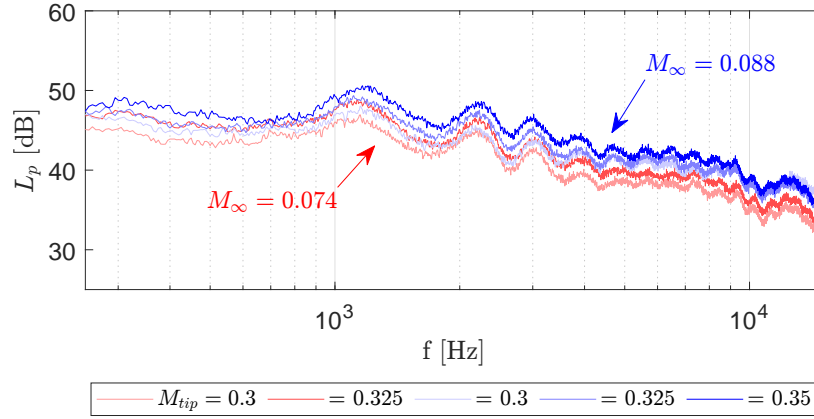


**Fig. 8** Sound pressure level ( $L_p$ ) spectra of the broadband component of the far-field noise recorded by a microphone at  $\vartheta = 140^\circ$  for grid C and all propeller operating conditions considered (see Table 2). **Red** shades correspond to  $M_\infty = 0.074$ , **blue** shades to  $M_\infty = 0.088$ . Frequency resolution  $\Delta f = 5$  Hz and overlap ratio of 50%.

To better investigate this aspect, Figure 9 reports the normalized sound pressure level  $L_p^*$  with different definitions for the normalized frequency. The sound pressure level is normalized through the dynamic pressure at 70% of the blade span  $q_r$ :

$$L_p^* = L_p + 20 \log_{10} \left( \frac{Pref}{q_r} \right) \quad (11)$$

where:

$$q_r = \frac{1}{2} \rho_\infty V_r^2 = \frac{1}{2} \rho_\infty \left[ (0.7 R_p \Omega_s)^2 + V_\infty^2 \right] \quad (12)$$

with  $V_r$  the relative inflow velocity as seen by the blade at 70% of the blade span, neglecting any induced velocity effect. A collapse of the spectra for different propeller operative conditions would indicate a proportionality with the fourth power of the tip Mach number, i.e.  $S_{pp}^b \propto M_{tip}^4$ . It has to be stressed however that the dependence on other non-dimensional parameters (e.g.  $M_\infty$  and  $Re_{0.7}$ ) could lead to an imperfect collapse of the curves even though the proportionality with  $M_{tip}$  remains valid. The frequency is instead non-dimensionalized by different expressions to try and shed more light on the physical mechanisms possibly influencing the phenomenon.

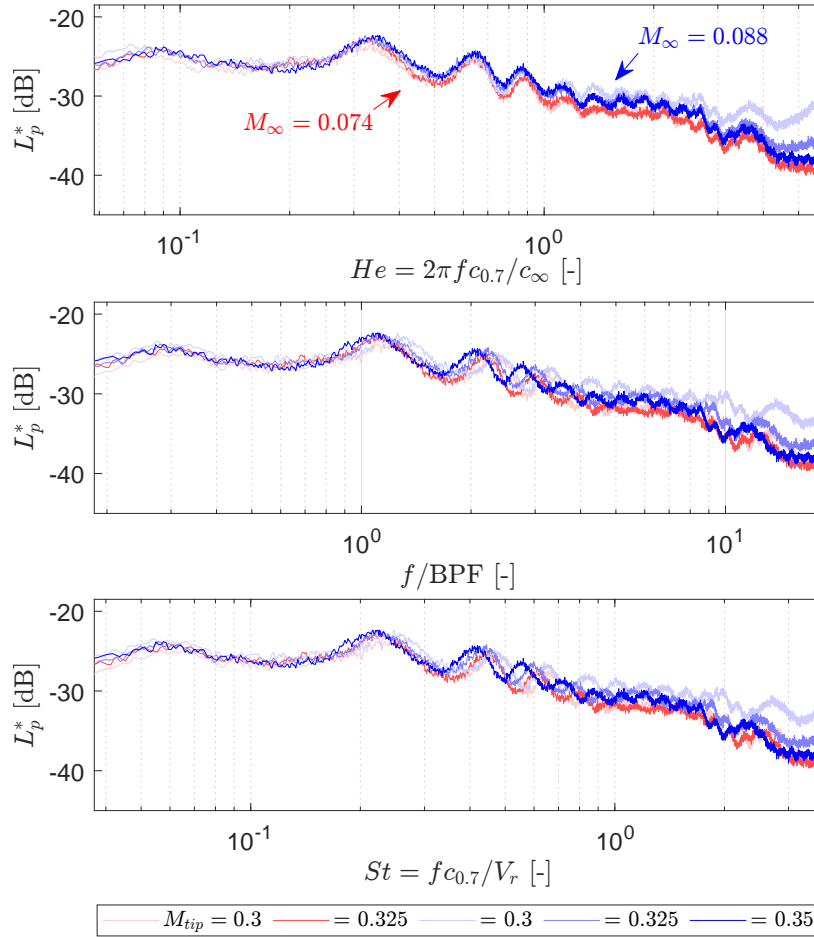


**Fig. 9** Normalized sound pressure level ( $L_p^*$ ) spectra of the broadband component of the far-field noise recorded by a microphone at  $\vartheta = 140^\circ$  for grid C and all propeller operating conditions considered (see Table 2). From top to bottom, the frequency is normalized using the Helmholtz number  $He$ , the BPF, and the Strouhal number  $St$ . Red shades correspond to  $M_\infty = 0.074$ , blue shades to  $M_\infty = 0.088$ . Frequency resolution  $\Delta f = 5$  Hz and overlap ratio 50%.

In particular, the top plot of Figure 9 employs the Helmholtz number definition based on the ‘representative’ blade chord  $c_{0.7}$ , taken again at 70% of the blade span, i.e.  $He = 2\pi f c_{0.7}/c_\infty$ . This formulation highlights the effects of source compactness, as  $He \ll 1$  corresponds to sources with a characteristic length that is much smaller than the relative acoustic wavelength. The center plot of Figure 9 uses instead the normalization by the BPF already employed in the preceding section. This definition is useful to assess whether the observed ‘bumps’ are indeed due to the haystacking phenomenon, as if this were the case, the ‘bumps’ should align. Finally, the bottom plot of Figure 9 normalizes the frequency through the Strouhal number definition based on the same representative chord of the definition in  $He$  and on the same reference velocity used for  $q_r$ , i.e.  $St = f c_{0.7}/V_r$ . This parameter is fundamental whenever vortex shedding phenomena are involved, as it takes into account both the effects of the inflow velocity and the propeller’s rotational speed. An overall look at the three plots of Figure 9 shows that the best collapse between the spectra for the different test conditions occurs if the frequency is expressed as the Helmholtz number. This follows from the weak dependence of the frequency-related features on  $V_\infty$  and the BPF observed for the dimensional plot in Figure 8, since both  $c_{0.7}$  and  $c_\infty$  remain constant between the different tests. The collapse is particularly good for  $He < 1$ , while above this threshold, differences arise between the two streamwise velocities considered. Tests with  $M_\infty = 0.073$  still show a near-perfect collapse, while tests with  $M_\infty = 0.088$  exhibit diverging trends. The fact that the broadband ‘humps’ collapse in both frequency and amplitude indicates that turbulence-related ‘haystacking’ may likely not be the main cause of this feature. An alternative potential explanation lies with residual acoustic reflections, which could not be properly suppressed through the acoustic treatments of both grids and nozzle (see II). Finally, the worsening in the collapse between the

spectra for  $M_\infty = 0.088$  at  $He > 2$  might be due to a larger importance of trailing edge noise sources and reduced acoustic compactness.

The effect of varying the inflow turbulence to the propeller on the far-field noise emission spectra is reported in Figure 10. In particular, this shows the broadband sound pressure level spectra for the propeller operating at  $M_\infty = 0.088$  and  $M_{tip} = 0.325$  under varying inflow turbulence conditions as recorded by a microphone at  $\vartheta = 140^\circ$ . The frequency was normalized by the BPF for ease of discussion. It can be noticed that turbulence ingestion causes a large increase in the spectral energy with respect to the reference condition of clean flow. This is particularly true for frequencies below 10 BPF. Above this threshold, the differences between the turbulent inflow cases tend to disappear while the ‘grid-off’ case shows an opposing trend, gradually rising with frequency. Furthermore, a direct proportionality between the inflow turbulence and the rise in broadband noise is apparent. The fact that the broad ‘humps’ are also present for the clean inflow case further points to an interference effect due to the experimental setup.

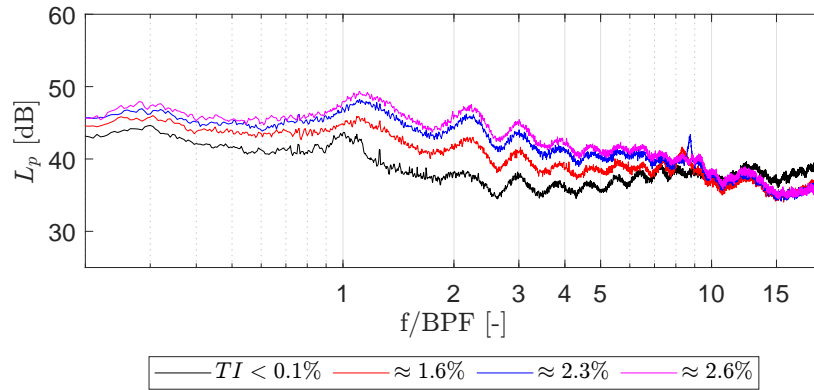


**Fig. 10** Sound pressure level ( $L_p$ ) spectra of the broadband component of the far-field noise recorded by a microphone at  $\vartheta = 140^\circ$  for a fixed propeller operating condition ( $M_\infty = 0.088$ ,  $M_{tip} = 0.325$ ) and all inflow turbulence cases considered.

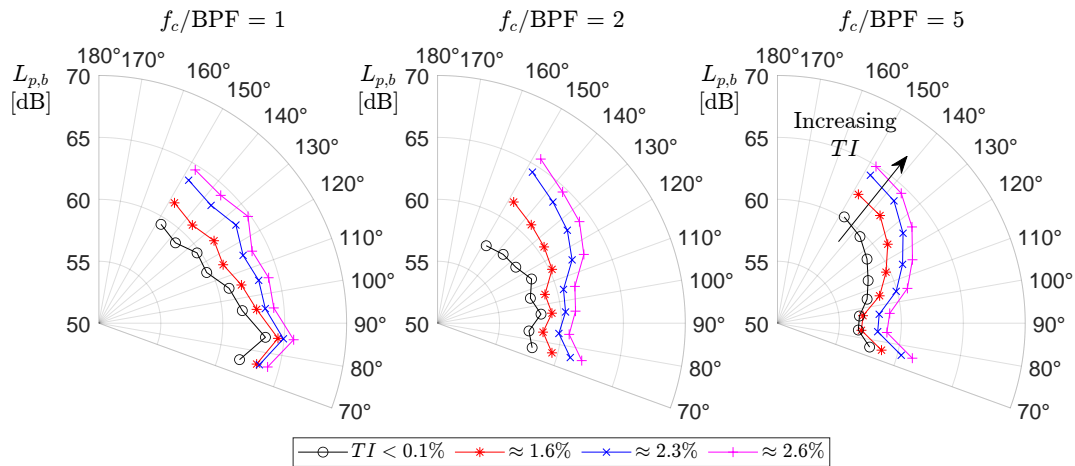


**Fig. 11** Radiation patterns of far-field broadband noise sound pressure level within one-third octave bands centered at different frequencies (left: 1 BPF, center: 2 BPF, right: 5 BPF) produced at a fixed propeller operating condition ( $M_\infty = 0.088$ ,  $M_{tip} = 0.325$ ) for all the considered turbulent inflow cases.

Figure 11 reports the directivity pattern of the sound pressure level within different frequency bands ( $L_{p,b}$ ) for varying levels of inflow turbulence for the same propeller operating conditions of Figure 10. This quantity is defined as:

$$L_{p,b} = 10 \log_{10} \left( \frac{P(f_c)}{p_{ref}^2} \right) \quad (13)$$

where  $f_c$  is the center frequency and  $P(f_c)$  is the acoustic power contained within the frequency band. The band's frequency bandwidth  $\Delta f = f_U - f_L$  is defined so that  $f_U = 2^{1/3} f_L$  and  $f_L = 2^{-1/6} f_c$ , i.e. a 1/3rd octave band centered around the frequency  $f_c$ . The plot reports the directivities at  $f_c/\text{BPF} = 1, 2$  and  $5$ , corresponding to the main frequency range for which Figure 10 shows the largest effect of turbulence ingestion. It can be seen that the ingestion of turbulence increases the values of  $L_{p,b}$  over the whole range of the polar angles considered and for all of the chosen center frequencies. The shape of the radiation pattern, instead, is highly dependent on this last parameter. In particular, at  $f_c/\text{BPF} = 1$  the maximum values of  $L_{p,b}$  tend to occur towards the propeller plane, i.e.  $\vartheta = 90^\circ$ . As the inflow turbulence increases, however, the directivity pattern flattens and tends to a more omnidirectional trend. In all the other cases (except for the 'clean' inflow at  $f_c/\text{BPF} = 2$ ), the maxima occur at the polar angle furthest downstream (i.e.  $\vartheta = 140^\circ$ ) while the minima are located in the propeller's plane. This change in the shape of the radiation pattern can be partially explained by the decrease in blade acoustic compactness ( $He \ll 1$ ) for increasing frequencies, as the chosen frequencies correspond, respectively, to  $He \approx 0.3, 0.6$  and  $1.5$ . Raposo & Azarpeyvand [44] reported a similar frequency-dependent directivity for an open propeller ingesting homogeneous and isotropic turbulence after applying the original model by Amiet [15].

### 3. Time-frequency domain analysis

The previous discussion focused on the time-averaged characteristics of the broadband noise emissions by the turbulence-ingesting propeller. Further insights can be obtained by considering the combined time- and frequency-domain information provided by the wavelet transform (see III.C).

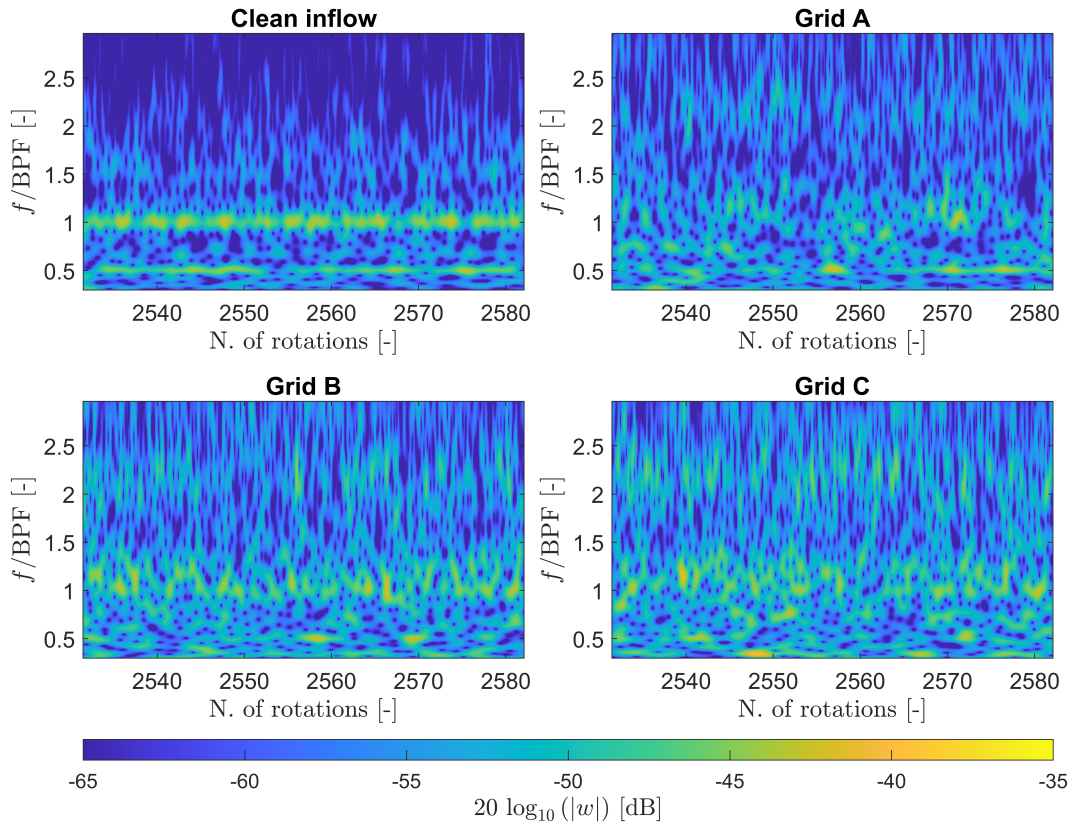


**Fig. 12** Squared modulus of wavelet coefficients for a fixed propeller operating condition ( $M_\infty = 0.073$ ,  $M_{tip} = 0.325$ ) and all the considered turbulent inflow cases. Microphone at  $\vartheta = 140^\circ$ . Complex Morlet wavelet ( $\omega_0 = 15$ ). Haystacking parameter values  $\chi = 2.3, 3$  and  $3.2$  for grids A, B and C respectively.

Figure 12 reports the time-frequency distribution of the squared modulus of the continuous wavelet transform  $w$  of the microphone signal at  $\vartheta = 140^\circ$  obtained for a fixed propeller operating condition ( $M_\infty = 0.073$ ,  $M_{tip} = 0.325$ ) and all the considered turbulent inflow cases. This choice corresponds to the highest values of the ‘haystacking parameter’ amongst the tested conditions (Table 3), indicating a higher likelihood of multiple blade interactions with the same turbulent structure. The analysis is performed on the unfiltered signal, containing both the tonal and broadband noise contributions. The analysed segment has a length of 0.3 s, corresponding to about 50 propeller rotations. Its location within the recorded time history was chosen arbitrarily. The frequency-dependent trade-off between frequency and time resolution characteristic of the CWT is evident. In particular, the choice of a base wavelet frequency  $\omega_0 = 15$  leads to a balance between the two at around the BPF, while temporal resolution gradually increases at the expense of the frequency resolution for higher values of  $f/\text{BPF}$ . It is clear that the clean inflow condition leads to a concentration of the acoustic emissions around the first BPF. Furthermore, a possible low-frequency modulation in the wavelet amplitude is also observed in this case. Turbulence, instead, is responsible for a great increase in the wavelet amplitude for  $f/\text{BPF} > 1$  when compared to the ‘grid off’ case. At the same time, the ‘tonal’ concentration of energy, which was observed in the baseline case, seems to either lack (grid A) or be more discontinuously distributed in time. In addition, the ‘broadband’ signal is seen to be the result of a large number of short-duration pulses spanning a broad frequency range. These pulses may possibly arise from the interaction of the blades with the turbulent structures present in the inflow, since both their frequency of occurrence and the relative wavelet amplitudes tend to increase with increasing inflow turbulence levels.

## V. Conclusions

The present paper dealt with an experimental investigation of turbulence ingestion noise by an isolated scale-model propeller. The use of SMSB grids with varying mesh sizes placed upstream of a slight contraction allowed for evaluating the effects of increasing turbulence inflow levels on the noise emissions of the propeller. Tonal/broadband noise separation techniques were employed to isolate the contribution most likely related to turbulence ingestion (i.e. leading edge noise), which is an inherently broadband phenomenon. In particular, a combination of phase-averaging (EA) and phase-shifting (Sree’s method) techniques permitted a further improvement in the determination of the incoherent component, removing residual tones unrelated to the propeller’s shaft frequency (e.g. wind tunnel operation and electric motor). The same techniques were also applied to suppress the hydrodynamic near-field coherent contributions present in hot-wire signals, enabling a partial characterization of the turbulence being ingested by the propeller. The main findings of the study can be summarized as follows:

- The broadband noise emissions for a fixed inflow turbulence condition scale with the fourth power of the tip Mach number (i.e.  $S_{pp}^b \propto M_{tip}^4$ ) for Helmholtz numbers lower than unity. Differences in the collapse of the spectra, however, arise between the different tested  $M_\infty$  for higher values of  $He$ ;
- Turbulence ingestion does not appreciably affect the induction velocity caused by the propeller at  $0.15R_p$  upstream of the propeller’s disk. At the same time, broadband noise emissions show large increases for non-dimensional frequencies  $f < 10 \text{ BPF}$  ( $He \lesssim 3$ );
- The broadband noise radiation pattern is highly dependent on the scaled frequency. In particular, the propeller shows a dipole-like directivity pattern with minima in the propeller plane for  $1/3$ -octave bands centered around  $f_c/\text{BPF} = 2$  and  $5$ . The radiation maxima are instead in the propeller plane for  $f_c/\text{BPF} = 1$ . Turbulence ingestion seems to affect the directivity pattern shapes as well, with increasing turbulence intensity values leading to a more omnidirectional trend for  $f_c/\text{BPF} = 1$ ;
- A time-frequency domain analysis through the CWT technique has shown that the broadband noise emissions arise from a large number of short-duration pulses with a frequency content spanning a large range. This was possibly linked to the interaction of the propeller with the single turbulent structures present in the flow.

Future work should aim at further extending the ranges of the non-dimensional parameters  $M_\infty$  and  $M_{tip}$  considered in the present campaign. Furthermore, the effects of propeller geometry (e.g. blade number and blade pitch angle) could also be further investigated at constant  $M_\infty$  and  $M_{tip}$  to gain insight into the influence of blade loading on turbulence ingestion noise.

## Acknowledgments

The authors would like to thank Dr. S. Satish Kumar, Amy Morin, Fernanda do Nascimento Monteiro, and Carlos Orce López for their assistance in setting up and running the experiment. Special thanks also to Andrea Piccolo, Prof. Daniele Ragni, and Dr. Riccardo Zamponi for their valuable discussions and insights on the results.

## Funding Sources

This work is part of the HOPE (Hydrogen Optimized multi-fuel Propulsion system for clean and silEnt aircraft) project, and has received funding from the European Union's Horizon Europe research and innovation programme under grant agreement No. 101096275. Additionally, this publication is also a part of the *Listen to the future* project (project number 20247), a part of the Veni 2022 research programme (Domain Applied and Engineering Sciences). The latter project is granted to Roberto Merino-Martinez and is (partially) financed by the Dutch Research Council (NWO).

## References

- [1] De Vries, R., Van Arnhem, N., Sinnige, T., Vos, R., and Veldhuis, L. L., "Aerodynamic interaction between propellers of a distributed-propulsion system in forward flight," *Aerospace Science and Technology*, Vol. 118, 2021, p. 107009. <https://doi.org/10.1016/j.ast.2021.107009>.
- [2] Della Corte, B., Van Sluis, M., Gangoli Rao, A., and Veldhuis, L. L. M., "Aerodynamic Performance of an Aircraft with Aft-Fuselage Boundary-Layer-Ingestion Propulsion," *Journal of Aircraft*, Vol. 59, No. 4, 2022, pp. 1054–1070. <https://doi.org/10.2514/1.C036596>.
- [3] Gudmundsson, S., "The Anatomy of the Propeller," *General Aviation Aircraft Design*, Elsevier, 2014, pp. 581–659. <https://doi.org/10.1016/B978-0-12-397308-5.00014-3>.
- [4] Hassanalain, M., and Abdelkefi, A., "Classifications, applications, and design challenges of drones: A review," *Progress in Aerospace Sciences*, Vol. 91, 2017, pp. 99–131. <https://doi.org/10.1016/j.paerosci.2017.04.003>.
- [5] Roger, M., and Moreau, S., "Tonal-Noise Assessment of Quadrotor-Type UAV Using Source-Mode Expansions," *Acoustics*, Vol. 2, No. 3, 2020, pp. 674–690. <https://doi.org/10.3390/acoustics2030036>.
- [6] Torija, A. J., and Nicholls, R. K., "Investigation of Metrics for Assessing Human Response to Drone Noise," *International Journal of Environmental Research and Public Health*, Vol. 19, No. 6, 2022, p. 3152. <https://doi.org/10.3390/ijerph19063152>.
- [7] Merino-Martinez, R., Ben-Gida, H., and Snellen, M., "Psychoacoustic Evaluation of an Optimized Low-Noise Drone Propeller Design," 30<sup>th</sup> *International Congress on Sound and Vibration (ICSV), July 8 – 11 2024, Amsterdam, the Netherlands*, 2024.
- [8] Merino-Martinez, R., Yupa-Villanueva, R. M., von den Hoff, B., and Pockel , J. S., "Human response to the flyover noise of different drones recorded in field measurements," 3<sup>rd</sup> *Quiet Drones conference, September 8 – 11 2024, Manchester, United Kingdom*, 2024.
- [9] Van Arnhem, N., De Vries, R., Sinnige, T., Vos, R., Eitelberg, G., and Veldhuis, L. L. M., "Engineering Method to Estimate the Blade Loading of Propellers in Nonuniform Flow," *AIAA Journal*, Vol. 58, No. 12, 2020, pp. 5332–5346. <https://doi.org/10.2514/1.J059485>.
- [10] Tinney, C. E., and Sirohi, J., "Multicopter Drone Noise at Static Thrust," *AIAA Journal*, Vol. 56, No. 7, 2018, pp. 2816–2826. <https://doi.org/10.2514/1.J056827>.
- [11] Jamaluddin, N. S., Celik, A., Baskaran, K., Rezgui, D., and Azarpeyvand, M., "Experimental analysis of a propeller noise in turbulent flow," *Physics of Fluids*, Vol. 35, No. 7, 2023, p. 075106. <https://doi.org/10.1063/5.0153326>.
- [12] Zaman, I., Falsi, M., Zang, B., Azarpeyvand, M., and Camussi, R., "Aeroacoustics of the propeller Boundary Layer Ingestion configuration for varying thrusts," *Journal of Sound and Vibration*, Vol. 589, 2024, p. 118604. <https://doi.org/10.1016/j.jsv.2024.118604>.
- [13] Hubbard, H. H., "Aeroacoustics of Flight Vehicles: Theory and Practice Volume 1: Noise Sources," Tech. Rep. 19920001380, NASA , 1991.
- [14] Glegg, S. A. L., and Devenport, W. J., *Aeroacoustics of low Mach number flows: fundamentals, analysis, and measurement*, Academic Press, London, 2017.

- [15] Amiet, R. K., "Noise produced by turbulent flow into a rotor: theory manual for noise calculation," Contractor report 181788, NASA , 1989.
- [16] Bowen, L., Celik, A., and Azarpeyvand, M., "A thorough experimental investigation on airfoil turbulence interaction noise," *Physics of Fluids*, Vol. 35, No. 3, 2023, p. 035123. <https://doi.org/10.1063/5.0142704>.
- [17] Blandeau, V. P., and Joseph, P. F., "Validity of Amiet's Model for Propeller Trailing-Edge Noise," *AIAA Journal*, Vol. 49, No. 5, 2011, pp. 1057–1066. <https://doi.org/10.2514/1.J050765>.
- [18] Sevik, M., "Sound Radiation from a Subsonic Rotor Subjected to Turbulence," *Fluid Mech., Acoustics, and Design of Turbomachinery, Pt. 2*, 1974.
- [19] Alexander, W., Devenport, W. J., and Glegg, S. A., "Noise from a rotor ingesting a thick boundary layer and relation to measurements of ingested turbulence," *Journal of Sound and Vibration*, Vol. 409, 2017, pp. 227–240. <https://doi.org/10.1016/j.jsv.2017.07.056>.
- [20] Grande, E., Romani, G., Ragni, D., Avallone, F., and Casalino, D., "Aeroacoustic Investigation of a Propeller Operating at Low Reynolds Numbers," *AIAA Journal*, Vol. 60, No. 2, 2022, pp. 860–871. <https://doi.org/10.2514/1.J060611>.
- [21] Huff, D. L., and Henderson, B. S., "Electric Motor Noise for Small Quadcopters: Part 1 – Acoustic Measurements," *2018 AIAA/CEAS Aeroacoustics Conference*, American Institute of Aeronautics and Astronautics, Atlanta, Georgia, 2018. <https://doi.org/10.2514/6.2018-2952>.
- [22] Metzger, F. B., "An assessment of propeller aircraft noise reduction technology," Contractor Report (CR) NIPS-95-06245 , 1995.
- [23] Bonomo, L. A., Cordioli, J. A., Colaciti, A. K., Fonseca, J. V. N., and Simões, L. G., "Assessment of the Performance of Tonal-Broadband Decomposition Algorithms for Propeller Noise," *AIAA AVIATION 2023 Forum*, American Institute of Aeronautics and Astronautics, San Diego, CA and Online, 2023. <https://doi.org/10.2514/6.2023-3218>.
- [24] Sree, D., "A Novel Signal Processing Technique for Separating Tonal and Broadband Noise Components from Counter-Rotating Open-Rotor Acoustic Data," Vol. 12, No. 1, 2013.
- [25] Sree, D., and Stephens, D., "Improved Separation of Tone and Broadband Noise Components from Open Rotor Acoustic Data," *Aerospace*, Vol. 3, No. 3, 2016, p. 29. <https://doi.org/10.3390/aerospace3030029>.
- [26] Daubechies, I., *Ten Lectures on Wavelets*, Society for Industrial and Applied Mathematics, 1992. <https://doi.org/10.1137/1.9781611970104>.
- [27] Meloni, S., De Paola, E., Grande, E., Ragni, D., Stoica, L. G., Di Marco, A., and Camussi, R., "A wavelet-based separation method for tonal and broadband components of low Reynolds-number propeller noise," *Measurement Science and Technology*, Vol. 34, No. 4, 2023, p. 044007. <https://doi.org/10.1088/1361-6501/acb071>.
- [28] Camussi, R., and Iemma, U., "Advanced Processing Techniques and Data Assimilation," *Lecture Series Notes: Measurement, Modelling and Simulations Techniques for the Design and Development of Novel Aircraft Architectures*, Von Karman Institute for Fluid Mechanics, Sint-Genesius-Rode, Belgium, 2024.
- [29] Merino-Martínez, R., Rubio Carpio, A., Lima Pereira, L. T., Van Herk, S., Avallone, F., Ragni, D., and Kotsonis, M., "Aeroacoustic design and characterization of the 3D-printed, open-jet, anechoic wind tunnel of Delft University of Technology," *Applied Acoustics*, Vol. 170, 2020, p. 107504. <https://doi.org/10.1016/j.apacoust.2020.107504>.
- [30] Quaroni, L. N., Merino-Martínez, R., Monteiro, F. D., and Kumar, S. S., "Collective blade pitch angle effect on grid turbulence ingestion noise by an isolated propeller," *30th AIAA/CEAS Aeroacoustics Conference (2024)*, American Institute of Aeronautics and Astronautics, Rome, Italy, 2024. <https://doi.org/10.2514/6.2024-3209>.
- [31] van Arnhem, N., de Vries, R., Sinnige, T., and Veldhuis, L., "TUD-XPROP-S propeller geometry," , Mar. 2022. <https://doi.org/10.5281/ZENODO.6355670>.
- [32] Comte-Bellot, G., and Corrsin, S., "The use of a contraction to improve the isotropy of grid-generated turbulence," *Journal of Fluid Mechanics*, Vol. 25, No. 4, 1966, pp. 657–682. <https://doi.org/10.1017/S0022112066000338>.
- [33] Bowen, L., Celik, A., Azarpeyvand, M., and Da Silva, C. R. I., "Grid Generated Turbulence for Aeroacoustic Facility," *AIAA Journal*, Vol. 60, No. 3, 2022, pp. 1833–1847. <https://doi.org/10.2514/1.J060851>.

- [34] Li, L., Zhu, H., Maryami, R., Zhang, X., and Liu, Y., "Flow and acoustic characterization of turbulence grids at wind tunnel nozzle exit," *Journal of Sound and Vibration*, Vol. 590, 2024, p. 118535. <https://doi.org/10.1016/j.jsv.2024.118535>.
- [35] Quaroni, L. N., and Merino-Martínez, R., "Aeroacoustic characterization of acoustically-treated turbulence grids in axisymmetric contraction for open-jet wind tunnels," *2025 AIAA AVIATION Forum*, Las Vegas, USA, 2025.
- [36] Amiet, R., "Correction of open jet wind tunnel measurements for shear layer refraction," *2nd Aeroacoustics Conference*, American Institute of Aeronautics and Astronautics, Hampton, VA, U.S.A., 1975. <https://doi.org/10.2514/6.1975-532>.
- [37] O'Meara, M. M., and Mueller, T. J., "Laminar separation bubble characteristics on an airfoil at low Reynolds numbers," *AIAA Journal*, Vol. 25, No. 8, 1987, pp. 1033–1041. <https://doi.org/10.2514/3.9739>.
- [38] Fyfe, K., and Munck, E., "Analysis of Computed Order Tracking," *Mechanical Systems and Signal Processing*, Vol. 11, No. 2, 1997, pp. 187–205. <https://doi.org/10.1006/mssp.1996.0056>.
- [39] Addison, P. S., *The illustrated wavelet transform handbook: introductory theory and applications in science, engineering, medicine and finance*, Taylor & Francis, New York, 2002. <https://doi.org/10.1201/9781420033397>.
- [40] Torrence, C., and Compo, G. P., "A Practical Guide to Wavelet Analysis," *Bulletin of the American Meteorological Society*, Vol. 79, No. 1, 1998, pp. 61–78. [https://doi.org/10.1175/1520-0477\(1998\)079<0061:APGTWA>2.0.CO;2](https://doi.org/10.1175/1520-0477(1998)079<0061:APGTWA>2.0.CO;2).
- [41] Bendat, J. S., and Piersol, A. G., *Engineering applications of correlation and spectral analysis*, 2<sup>nd</sup> ed., A Wiley-Interscience publication, Wiley, New York, 1993.
- [42] Go, S. T., Kingan, M. J., Bowen, L., and Azarpeyvand, M., "Noise of a shrouded propeller due to ingestion of grid-generated turbulence," *Journal of Sound and Vibration*, 2023, p. 118044. <https://doi.org/10.1016/j.jsv.2023.118044>.
- [43] Roach, P., "The generation of nearly isotropic turbulence by means of grids," *International Journal of Heat and Fluid Flow*, Vol. 8, No. 2, 1987, pp. 82–92. [https://doi.org/10.1016/0142-727X\(87\)90001-4](https://doi.org/10.1016/0142-727X(87)90001-4).
- [44] Raposo, H., and Azarpeyvand, M., "Turbulence ingestion noise generation in rotating blades," *Journal of Fluid Mechanics*, Vol. 980, 2024, p. A53. <https://doi.org/10.1017/jfm.2024.7>.